

EJBot-II: an optimized skid-steering propeller-type climbing robot with transition mechanism

Mohamed G. Alkalla, Mohamed A. Fanni, Abdel- Fattah Mohamed, Shuji Hashimoto, Hideyuki Sawada, Takanobu Miwa & Amr Hamed

To cite this article: Mohamed G. Alkalla, Mohamed A. Fanni, Abdel- Fattah Mohamed, Shuji Hashimoto, Hideyuki Sawada, Takanobu Miwa & Amr Hamed (2019): EJBot-II: an optimized skid-steering propeller-type climbing robot with transition mechanism, Advanced Robotics, DOI: [10.1080/01691864.2019.1657948](https://doi.org/10.1080/01691864.2019.1657948)

To link to this article: <https://doi.org/10.1080/01691864.2019.1657948>



[View supplementary material](#)



Published online: 29 Aug 2019.



[Submit your article to this journal](#)



[View related articles](#)



[View Crossmark data](#)



EJBot-II: an optimized skid-steering propeller-type climbing robot with transition mechanism

Mohamed G. Alkalla ^{a*}, Mohamed A. Fanni ^{b*}, Abdel-Fattah Mohamed ^{b†}, Shuji Hashimoto ^c, Hideyuki Sawada ^c, Takanobu Miwa ^c and Amr Hamed ^b

^aSurrey Space Centre, University of Surrey, Guildford, UK; ^bMechatronics and Robotics Engineering Department, Egypt–Japan University of Science and Technology (E-JUST), Alexandria, Egypt; ^cDepartment of Applied Physics, School of Advanced Science and Engineering, Waseda University, Tokyo, Japan

ABSTRACT

This paper presents a new kind of climbing robots called EJBot, which has not been restricted to climb certain surface materials or terrains. EJBot is inspired by propeller-based aviation systems, however, its adhesion principle is opposite to flight concept. Thanks to the hybrid actuation system embedded in this robot which gives a good and stable adhesion. This hybrid system consists of propeller thrust forces and wheel torques actuated simultaneously to generate the proper adhesion force. It is similar to a car climbing a ramp, it needs both weight of the car and the wheels' torques. Without these torques, the car will roll down. Consequently, the thrust forces of the propellers increase the traction force capacity, then the wheels' role arises to generate the convenient torques for stopping the robot or navigating it on the structures. The feasibility of this adhesion concept is verified by the first and second modules of EJBot as presented in the simulation and practical results.

ARTICLE HISTORY

Received 26 December 2018
Revised 11 June 2019
Accepted 8 August 2019

KEY WORDS

Climbing robot; propeller; traction forces; adhesion forces; skid-steering climbing robot (SSCR).

1. Introduction

In the last few years there has been a growing interest in the climbing robots for several civilian and industrial fields. Its importance stands out from the vital applications which are very dangerous for the human to perform himself, such as, cleaning glass facades, inspection of tanks, vessels, ships welds, nuclear power plants and highway bridges. In addition to climbing high buildings for rescue and exploration purposes. This work is an extension to simulation and experimental works performed previously for the propeller-type climbing robot (EJBot-I, Figure 1) in [1–3]. Hence, this article presents an advanced and optimized model of EJBot to enhance the performance of the previous prototype. The main target of EJBot is to climb outer and inner vessels surfaces of the petrochemical and liquefied gas companies for a wireless visual inspection of welds' corrosion and wall thickness measurement. This process is essential for the regular inspection of these tanks. EJBot utilizes an innovative adhesion principle based on a hybrid actuation system. This hybrid system consists of propeller thrust forces and wheel torques, both should be actuated

simultaneously to generate the necessary adhesion force either to stop the robot or move it on any inclined surface. This adhesion system can be classified as an aerodynamic adhesion system, however, it does not require smooth surfaces like suction cups [4–9] and suction chambers [10–12] or proximity to the climbed surfaces like, vortex/impeller based adhesion systems [13–16]. Moreover, the proposed adhesion system is not influenced by holes, cracks, protrusions, or even surface curvature. Therefore, this adhesion system has advantage of generality of the climbed surface materials and terrains. Moreover, EJBot outperforms the other propeller-type climbing robots [17–19] in some aspects such as, control simplicity and navigation stability, as discussed in [3], since these robots were using propellers only as the lone source of generating adhesion force.

2. EJBot-I model

Design of EJBot-I comprises two coaxial upturned propellers mounted on a mobile platform with four standard actuated wheels. The propellers generate thrust forces

CONTACT Mohamed Alkalla m.alkalla@surrey.ac.uk Surrey Space Centre, University of Surrey, GU27XH Guildford, UK

*On leave: Production Engineering & Mechanical Design Dept., Faculty of Engineering, Mansoura University, Egypt, m_elkalla@mans.edu.eg.

†On leave: Department of Electrical and Electronics Engineering, Assiut University, Egypt.

Supplemental data for this article can be accessed here. <https://doi.org/10.1080/01691864.2019.1657948>



Figure 1. EJBot-I in different climbing scenarios. (a) Climbing outer cylindrical surface of concrete pipe. (b) Navigating the ceiling.

which provide a normal force capacity on each wheel. By increasing the normal force capacity, the traction force capacity of the wheels is increased too. This allows the robot to attach strongly to any inclined surface. The robot has capabilities of climbing smooth and rough surfaces, inner and outer cylindrical surfaces like huge pipes, see Figure 1(a), and moving on the ceiling, see Figure 1(b). The average speed of the robot is nearly 250 mm/s and its payload capacity is 600 g. This value is enough to carry a wireless camera with lighting system, such as ‘TTL Serial JPEG Camera with NTSC Video and IR LEDs’, where its weight is 150 g only. The robot is efficiently tele-operated by a PS2 radio control unit. The experimental results show the robot’s ability to climb, explore, move in arbitrary directions on structures, and overcome significant obstacles up to 40 mm. EJBot-I shows a great ability to climb different types of surface materials and topologies. Moreover, it has a small weight and compact size, as well as simple control and good stability.

3. EJBot-II design and modeling

Although the several merits of EJBot-I, as mentioned formally, there are still some improvements to be performed, such as; applying the structural topology optimization and using a composite material for the robot frame to get a stiff and light-weight climbing robot, as well as, implementing a transition mechanism for transferring between the intersecting/orthogonal surfaces, particularly, the transition from ground to the walls. Another improvement is to mount the batteries directly on the robot and get rid of the umbilical cord. This will prevent many problems such as, excessive weight of the cord and hindering the robot motion. The last improvement is replacing the wheels with tracks system to get higher traction forces. These suggested improvements will be implemented in the new model which called EJBot-II.

3.1. Selection of the best design of EJBot-II

A transition mechanism is required to smoothly transfer between intersected/orthogonal surfaces. Many

alternatives are created to choose the best design among them based on certain criteria, such as, transition mechanism capability, number of actuations, robot size and weight, system stability, consumed power, control simplicity, traction capability, and overall climbing ability. The first design uses two arms to generate forces against the ground hence, the robot can raise up toward the vertical surface, see Figure 2(a). The advantages of this idea are compactness of robot size and simple control of arms, however, it requires a powerful transition arm motor to afford the total robot weight and propeller thrust forces. The second design depends on two modular tracked robots connected by an actuated revolute joint, as shown in Figure 2(b). The advantage of this design is the simplicity of transition control, although it has large size and weight, besides utilizing a lot of actuators which in turn, consume much power. The third design utilizes v-shape tracks with multi-wheels as a tractive system against the wall, hence it can climb upward, as shown in Figure 2(c). This design has a low number of actuators, but it has many drawbacks such as; low transition and traction capacity, large size, the center of mass is far away from the climbed surface, and the contact areas between the tracks and the surface are comparatively less than those in the previous designs. The fourth design uses large-diameter front track-wheels and a propeller tilting mechanism for generating upward thrust force which collaborated with traction forces of tracks to transit the robot from the ground to wall easily, as shown in Figure 2(d). There are three advantages of this design; firstly, the vertical component of the thrust force assists carrying the robot weight, secondly, few actuators are used, and finally, the robot can stop on the wall just by tilting the propeller axis backward without applying any wheel torques. The disadvantages of this design are; its control complexity and low navigation stability to some extent. The fifth transition design is based on aviation idea, where the robot is flying up and rotating its platform then reversing the rotation of the propellers to stick on the wall, as shown in Figure 2(e). The advantage of this design is obtaining a versatile ground-aerial-climbing robot, although

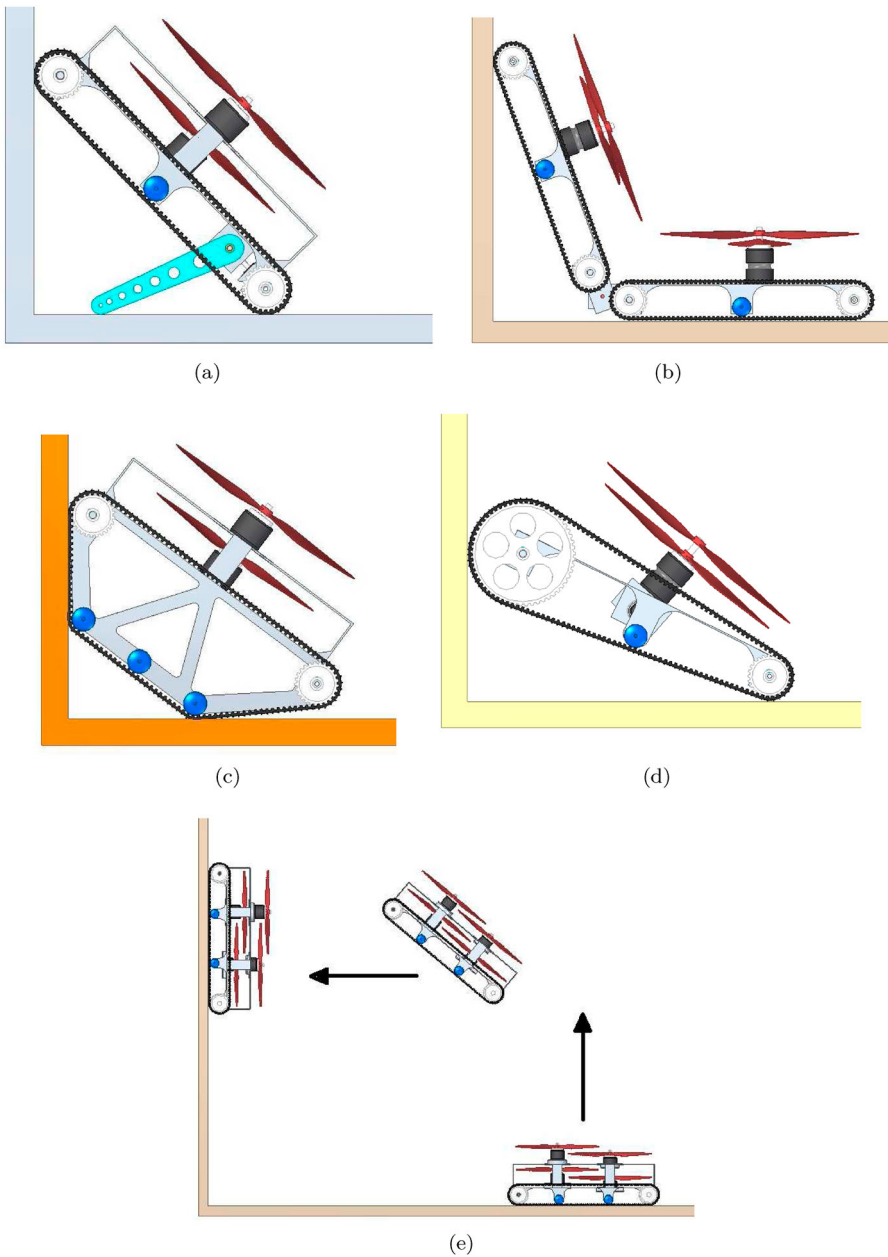


Figure 2. Different ideas of transition mechanisms for EJBot-II. (a) Design-I. (b) Design-II. (c) Design-III. (d) Design-IV. (e) Design V.

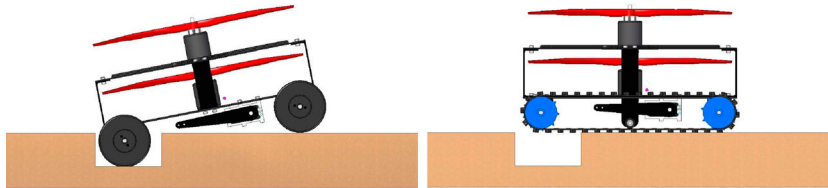
it has many drawbacks like; non-compact size, it needs sophisticated control means to switch between flying and climbing modes. Moreover, it needs at least four propellers to cancel their drag moment and to tilt the robot during flying. Finally, it may take some time for reversing the propellers rotation direction, in this meanwhile, the robot will fall down and get damaged. Table 1 presents a comparison between these alternatives to distinguish between them and choose the best and most feasible transition idea. The greater number of actuators, the more power consumption and weight will be. Therefore, it is a key factor in selecting the good design. Design-I may not

have the minimum number of motors but it has simpler control for transition and climbing rather than design-IV and design-V, on the other hand, design-III do not have good ability of transition or climbing particularly, if the wall is quite smooth. Besides, design-II is considered as a duplicated model (two robots attached to each other) with duplicated number of actuators, non-compact size and heavy weight. Therefore, design-I is the best one amongst them, due to its compactness, small weight, simple control, moderate power consumption, high traction capacity, good climbing ability, system stability, and fast transition mode. According to these preceding features,

Table 1. Comparison between different transition mechanism designs.

	Design-I	Design-II	Design-III	Design-IV	Design-V
No. of actuations*	6	9	4	5	6
Robot size	Compact	Not compact	Not compact	Compact	Not compact
Robot weight	Moderate	Heavy	Light	Moderate	Heavy
Control	Simple	Simple	Simple	Sophisticated	Sophisticated
Consumed power	Moderate	High	Low	Moderate	High
Traction capacity	High	High	Low	High	High
Climbing ability	Good	Good	Not good	Good	Good
Stability	Good	Good	Low	Low	Fair
Transition	Fast	Slow	Fast	Fast	Slow

including all propeller, wheel, arm or transition mechanism motors

**Figure 3.** Tracked robot can overcome large gaps.

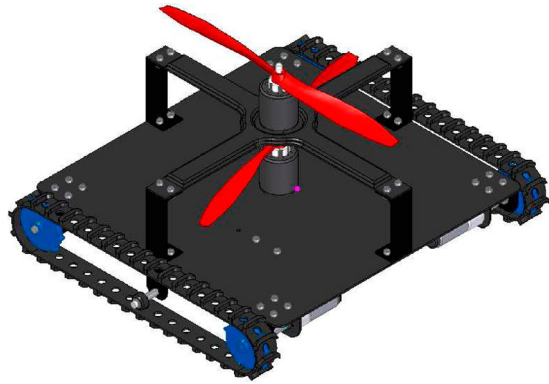
design-I is considered as the proposed design of EJBot-II. The improvements of this model are summarized as:

- (1) Using tracks system instead of wheels, since it provides more traction forces, and overcomes significant obstacles and large gaps easily, see Figure 3.
- (2) Minimizing the robot weight by using topology optimization technique, besides using carbon fiber reinforcement polymer (CFRP) instead of aluminum.
- (3) Mounting the batteries on the robot to avoid the umbilical cable problems, such as hindering the robot motion.
- (4) Adding the transition mechanism proposed in Design-I.

The CAD model of EJBot-II is created by SolidEdge ST8, as illustrated in Figure 4. In the first place, it is important to perform the structural topology optimization on the robot frame, where any excessive gram of weight consumes power from the battery and impedes the robot climbing ability.

3.2. Topology optimization of the robot frame

Topology optimization technique is used for optimizing the robot frame and minimizing its compliance. The continuous relative densities of the elements within the frame domain are used as the design variables. The topology optimization concept is mainly based on relocating the material within the frame domain to make the elements solid or void (empty), and hence, creating a model with various hole shapes and sizes. This phenomena is biologically inspired by the evolution of the bird wing bones depending on the load distribution on them, since the

**Figure 4.** CAD model of EJBot-II by Solid Edge ST8.

bones subjected to high loads have larger cross-section area with holes inside them rather than those subjected to small loads [20]. In this approach, the density and modulus of elasticity of the elements are expressed as follows:

$$\rho_i(x_i) = \rho_0 x_i, \quad E_i(x_i) = E_0 x_i^{p_n}, \quad (1)$$

$$0 < x_i \leq 1, \quad (2)$$

where x_i is the continuous relative density of each element, ρ_i and E_i are the material density and modulus of elasticity of each element, respectively. ρ_0 and E_0 are the initial density and modulus of elasticity of the frame material. p_n is a penalization power to penalize the intermediate densities and force them to become solid or empty (typically, $p_n \geq 3$ for poissos ratio equal to 1/3, according to Bendsoe [21]). Topology optimization technique is accomplished by using the method of moving asymptotes (MMA) as an optimization algorithm which

has been inspired by Svanberg [22]. The optimization problem is based on compliance minimization in (3) and subjected to constraints (4–6). The first constraint limits the final design mass and volume to a certain value, while the second constraint defines the stiffness equation used in the finite element analysis. The last constraint bounds the relative density of each element between 1 and x_{\min} as a small non-zero value to avoid singularity in matrix computations.

$$\min_x : C(\mathbf{x}) = \mathbf{U}^T K \mathbf{U} = \sum_{i=1}^n (x_i)^{p_n} u_i^T k_i u_i \quad (3)$$

$$\text{s.t.} : V(\mathbf{x})/V_0 = V_{frac}, \quad (4)$$

$$K \mathbf{U} = F, \quad (5)$$

$$0 < x_{\min} \leq x_i \leq 1, \quad (6)$$

where \mathbf{U} and F are the global displacement and force vectors, respectively; K is the global stiffness matrix, u_i and k_i are the element displacement vector and stiffness matrix, respectively; $V(\mathbf{x})$ and V_0 are the current iteration and the initial material volume, respectively; while V_{frac} is the prescribed volume fraction. For more details on the topology optimization technique, see [23], [24]. The initial design model with the boundary conditions and loads is shown in Figure 5, where there is a load equal to 24.52 N at the frame center applied by the lower propeller and a same load is distributed on the frame edges applied by the upper propeller. The maximum torque of each servo motor of the transition mechanism to raise the robot is 2100 N mm. These torques will exert on the frame. The wheel torques exerted on the frame are neglected comparing with the large torques applied by the transition arms, besides their nearness from the fixed corners. The frame is modeled in ANSYS, a finite element analysis (FEA) software, by SHELL181 element type as a 3D element with six DOFs. Firstly, the topology optimization technique is applied considering the propellers thrust force as the only load exerted on the frame. Then similarly, the transition arm torques are applied on the frame only, where the arms are not actuated continuously, just at the transition moments. The final optimum topological design will be obtained by gathering both optimum design shapes in the two cases with each other. By applying the thrust forces only on the frame, we get the optimum topological design, as shown in Figure 6(a). A comparison between the initial and final design results is given in Table 2. The results show that the compliance is reduced greatly from 1.149 to 0.105 N m. Similarly, the optimum topological design obtained from applying the torques only is shown in Figure 6(b), and its results are given in Table 3. Hence, the final optimum design of the robot frame considering both the thrust forces and

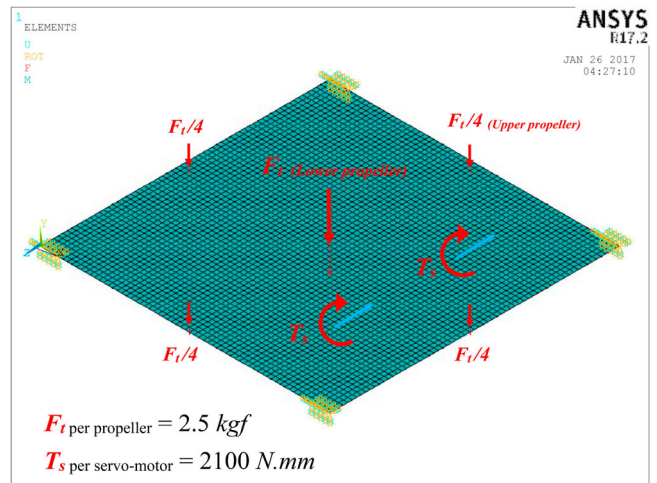


Figure 5. Initial design of the robot frame with the loads and boundary conditions.

torques is shown in Figure 7. These results are obtained at a volume fraction $V_{frac} = 0.35$.

3.3. EJBot-II force analysis

In this section, the optimum design is checked according to the strength and rigidity standpoints, moreover, the force analysis and the traction capacity are examined too. ANSYS is utilized to check the strength and rigidity of the frame design with loads and boundary conditions, as shown in Figure 5. The material of the frame is CFRP-T300 [25], and its properties are given in Table 4. The allowable stress is considered to be 1500 MPa. The FEA results are calculated, particularly for getting the maximum Von Mises stress and maximum displacement of the frame, hence, they are plotted in Figure 8. This figure shows that the maximum stress and displacement are 83.4 MPa and 1.73 mm, respectively. Therefore, the frame design is safe from the strength and rigidity viewpoints. Another FEA is performed for the assembled robot in the SolidEdge-ST8 CAD system with the aid of Femap for finite element modeling and NX Nastran solver technology. This analysis illustrates that the maximum stress and displacement are equal to 82.9 MPa and 1.27 mm, respectively, as shown in Figure 9. Consequently, the whole robot design is safe according to strength and rigidity criteria. All design parameters and robot specifications are summarized in Table 5. The static force analysis is performed for checking the traction capability of the robot during climbing, and hence the design validity. All forces and torques acting on the robot are illustrated in the free-body diagram in Figure 10. The equations' system which describes the equilibrium state of the robot on a surface with an

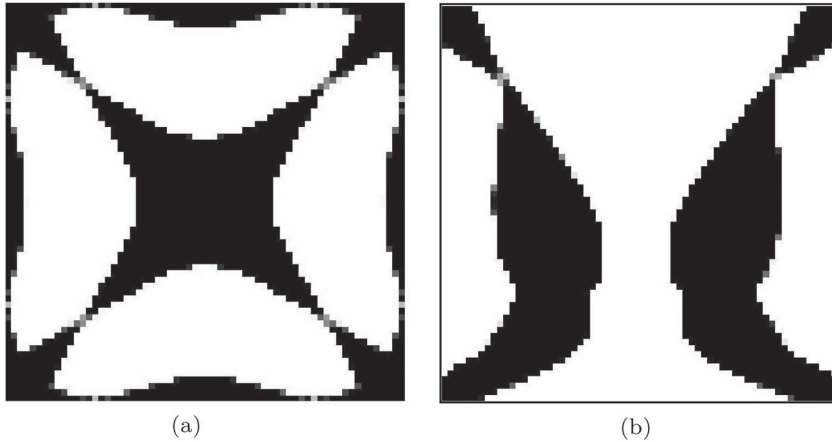


Figure 6. Optimum topological design of the frame. (a) Optimum design based on thrust forces only. (b) Optimum design based on the torques only.

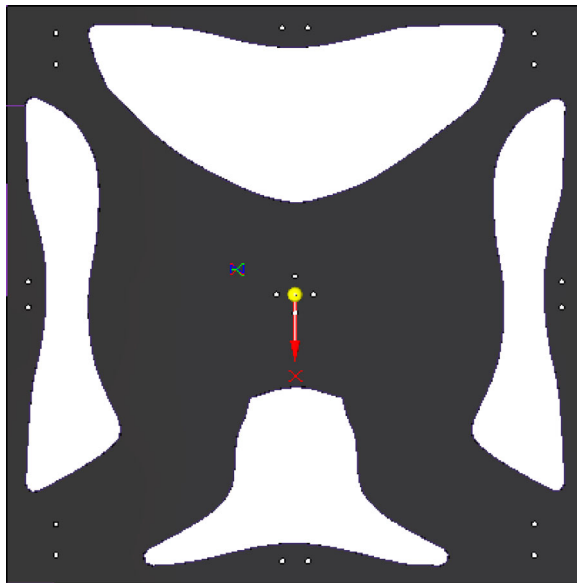


Figure 7. The final topological design of the robot frame.

Table 2. Results of topology optimization of the frame subjected to thrust forces only.

	Compliance (N·m)	Max. Deflection (m)	Max. Stress (MPa)
Initial Design	1.1490	0.0296	83.16
Optimum Design	0.1058	0.00279	127.13

Table 3. Results of topology optimization of the frame subjected to torques of the transition arms only.

	Compliance (N·m)	Max. Deflection (m)	Max. Stress (MPa)
Initial Design	3.0207	0.01894	134.438
Optimum Design	0.1866	0.00236	139.023

inclination angle ϕ is derived below:

$$\mathbf{AX} = \mathbf{B} \quad (7)$$

Table 4. Material properties of CFRP-T300, [25].

Properties	Value
Ultimate Tensile Strength	3530.39 MPa
Modulus of Elasticity	230.45 GPa
Density	1760 kg/m ³

where

$$\mathbf{X} = [F_{r1} \ F_{r2} \ F_{r3} \ F_{r4} \ F_{f1} \ F_{f2} \ F_{f3} \ F_{f4}]^T, \quad (8)$$

$$\mathbf{A} = \begin{bmatrix} 1 & 1 & 1 & 1 & 0 \\ 0 & 0 & 0 & 0 & 1 \\ 0 & 0 & 0 & 0 & -c \\ c & c & -c & -c & 0 \\ -(L-a) & a & -(L-a) & a & -(d+r) \\ 0 & 0 & 0 & 0 & 1 \\ 0 & 0 & 0 & 0 & 0 \\ 1/k_1 & -1/k_2 & -1/k_3 & 1/k_4 & 0 \\ 0 & 0 & 0 & 0 & 1 \\ 1 & 1 & 1 & 1 & 0 \\ -c & c & c & c & 0 \\ 0 & 0 & 0 & 0 & 1 \\ -(d+r) & -(d+r) & -(d+r) & -(d+r) & 0 \\ -1 & 0 & 0 & 0 & 1 \\ 0 & 1 & -1 & 0 & 0 \\ 0 & 0 & 0 & 0 & 1 \end{bmatrix} \quad (9)$$

$$\mathbf{B} = \begin{bmatrix} W \cos \phi + F_t & W \sin \phi & 0 & 0 \\ -F_t \left(\frac{L}{2} - a \right) & 0 & 0 & 0 \end{bmatrix}^T \quad (10)$$

where F_{ri} and F_{fi} are normal reaction force and frictional (tractive) force on wheel i respectively, F_t is the resultant propellers' thrust force, W is the robot weight, L is the longitudinal distance between the front and rear

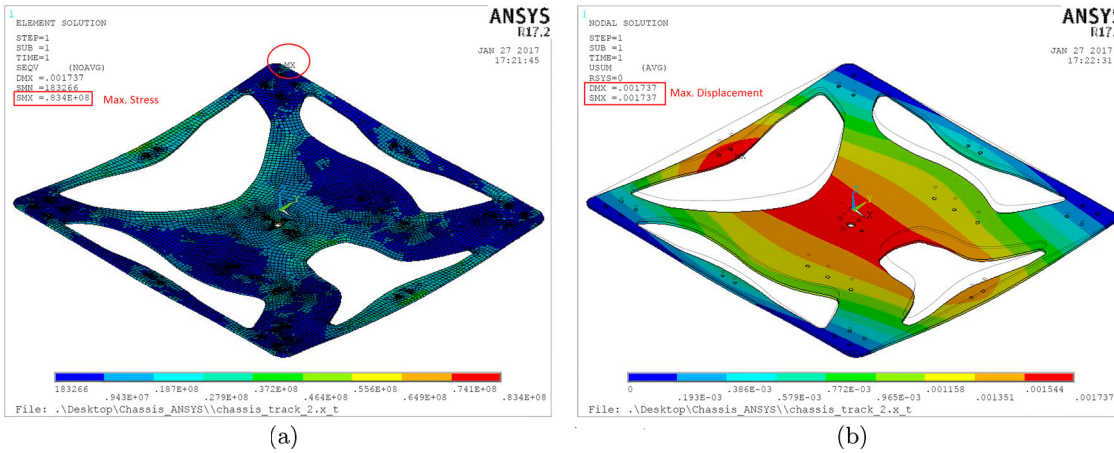


Figure 8. FEA by ANSYS R17.2 for the robot frame. (a) Stress analysis of the optimum topology frame design. (b) Displacement analysis of the optimum topology frame design.

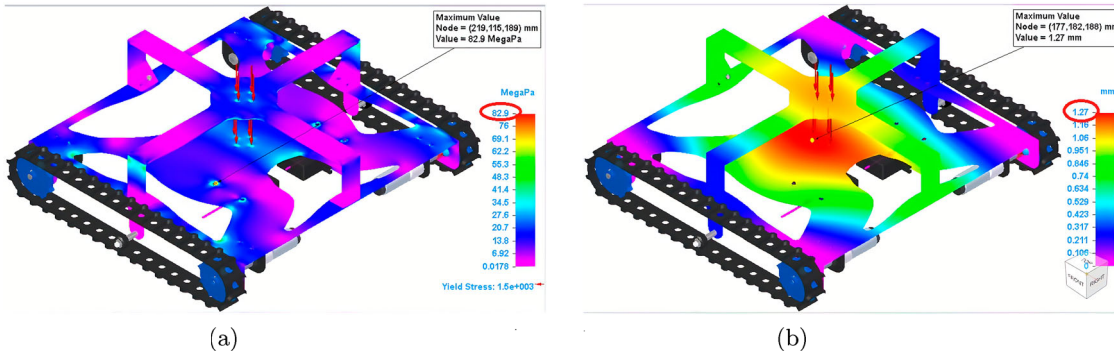


Figure 9. Finite element analysis of EJBot-II's chassis. (a) Stress analysis of EJBot-II. (b) Displacement analysis of EJBot-II.

wheel axles, c is the lateral distance between COM and the wheels, which is the half distance between the tracks (w), a is the longitudinal distance between COM and the rear wheels' axis, d is the orthogonal distance between COM and the plane which includes the four wheels' axes, r is the track wheel radius, and k_i is the stiffness of the track and wheel i . In case of using similar wheels and tracks, k_i will be omitted from (9). The robot can hold in its place or move with a constant velocity if the tractive force is less than the reaction force multiplied by the sliding static coefficient of friction, μ_s , as expressed in (11). This equation determines the capacity of the traction forces of the wheels at the non-slip condition, and provides an essential check to validate the robot design.

$$F_{fi} \leq \mu_s F_{ri} \quad \text{for } i = 1, \dots, 4 \quad (11)$$

This equation clarifies that the friction forces which interpreted into traction capacity of the robot do not depend only on the coefficient of friction between the tracks material and the wall, they also depend on the normal forces provided by the propeller. Hence, the drop of coefficient of friction can be compensated by the thrust forces. There are three propositions for this analysis:

Table 5. EJBot-II climbing robot specifications.

Properties	Value
Length between track wheel centers (L)	264 mm
Whole robot Length	324 mm
Width between the tracks (w)	346 mm
Whole robot width	371 mm
Frame thickness (t)	2 mm
Propeller diameter (D_p)	304 mm
Robot mass included 300 g battery (W)	1.750 kg
Material density of frame (CFRP) (ρ)	1760 kg/m ³
Max. thrust force (F_t)	49.05 N
Static friction coefficient (μ_s)	0.45
Tracks wheel radius (r)	30 mm
Orthogonal distance (d)	34 mm
Max. wheel motors torque (T_{max})	1.1277 N m
Max. transition arm servo motor torque	3.500 N m

- (1) Assume there is no slippage in the longitudinal direction of the tracks.
- (2) The equilibrium conditions are considered.
- (3) The wheels and tracks have the same size and material.

In the light of these propositions and former equations' system, the normal and tractive forces of the robot can be detected at any inclination angle of the

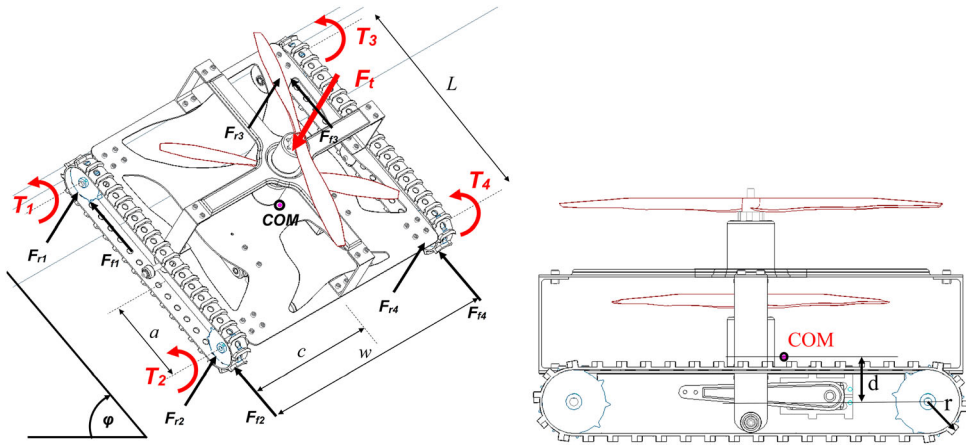


Figure 10. Free-body diagram of EJBot-II on inclined surface with angle ϕ .

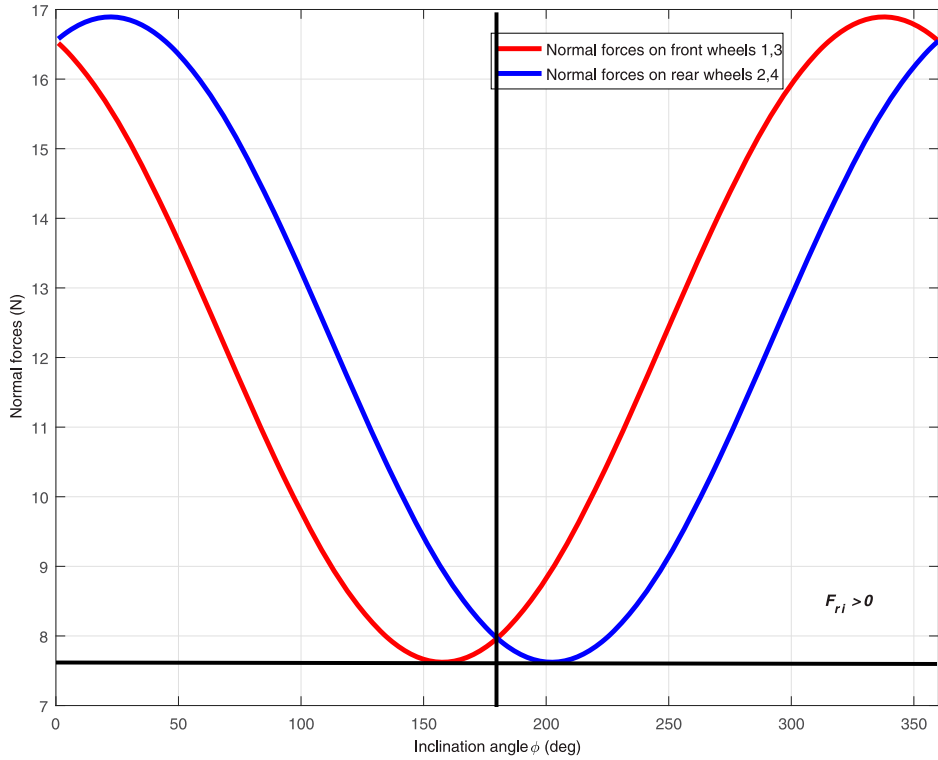


Figure 11. Normal forces on the front and rear track wheels vs. surface inclination angle.

climbed surfaces. Consequently, one can check/estimate the required torques of the driving motors that satisfy the non-slippage condition in (11), where the wheel torques are given as; $T_i = f_{fi} r_i$. The normal forces should be greater than zero to ensure the full contact between the tracks and the surface, as shown in Figure 11. The traction forces capacity of the robot is shown in Figure 12, where the solid (blue) and dotted (red) curves represent the maximum allowed tractive forces (traction capacity, equivalent to the right-hand side of (11)) at the front and rear track wheels, respectively. The dashed (black) curve represents the required tractive forces for the robot

tracks (equivalent to the left-hand side of (11)). These traction capacity should be greater than the required tractive forces, as shown in that figure. Hence the robot design is valid and there is no slippage, more details were explained in [3].

4. Analysis of transition mechanism

4.1. Ground-wall transition

It is necessary to study the actuation torques of the transition arms and the limitations on the robot rising angle

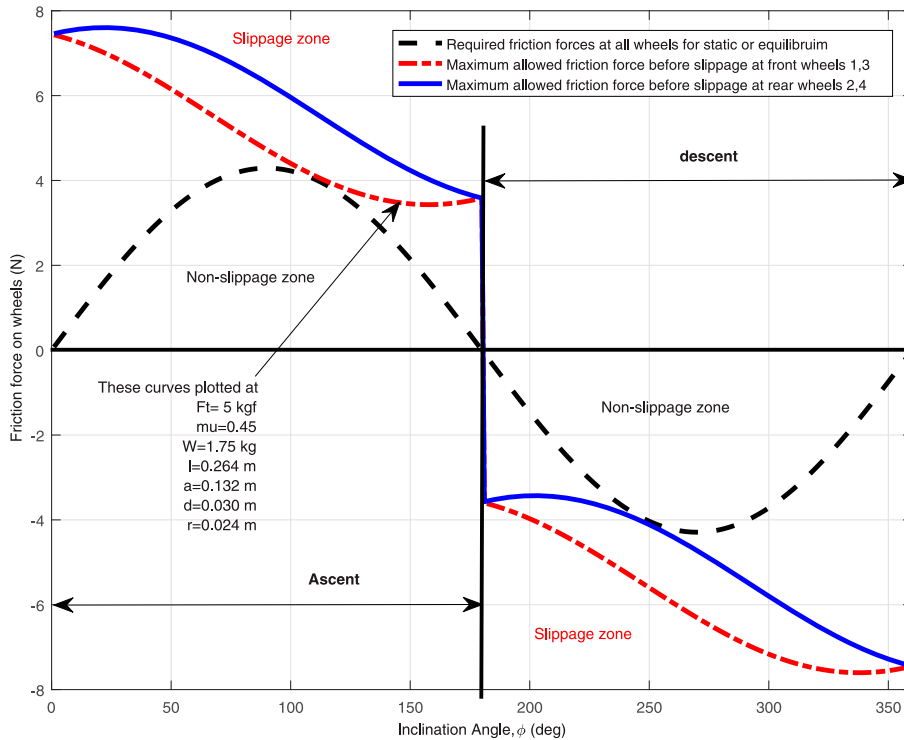


Figure 12. The required and maximum allowable tractive forces on the front and rear track wheels vs. surface inclination angle.

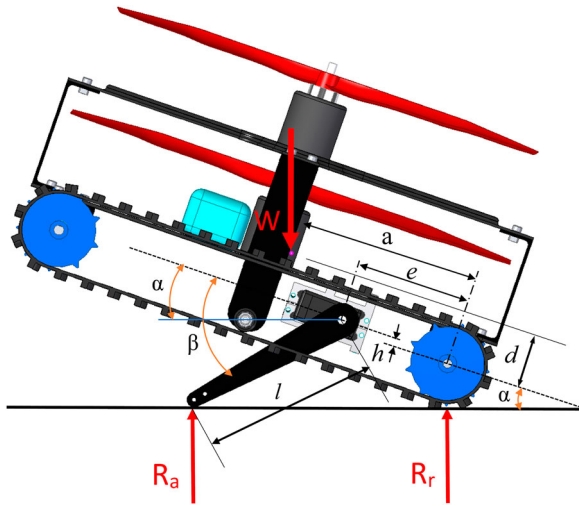


Figure 13. Transition arm analysis.

for appropriate selection of their motor. On the other hand, the investigation of accurate actuation that capable of lifting the robot is very crucial to avoid the excessive weight on the robot. The reaction forces on the front track wheels disappear when the robot on the verge of rising up from the ground, as shown in the free-body diagram in Figure 13. The propeller thrust forces are not required in the case of transiting between ground and wall. The robot rises up and moves to the wall, then the track with the propellers thrust forces will make the robot climb the wall. The analysis of the equilibrium condition

Table 6. Transition mechanism parameters.

Parameters	Value
COM distance (robot with 300 g battery) (a)	119 mm
COM distance (robot without battery) (a)	108 mm
Distance of arm motor (e)	73.1 mm
Transition arm length (l)	112.8 mm
Distance (h)	4.2 mm

requires studying the effect of ground on the transition arms and the track rear wheels, as derived in the following equations:

$$R_a + R_r = W, \quad (12)$$

$$- R_a[e \cos \alpha + l \cos(\beta - \alpha) - h \sin \alpha] \\ + W(a \cos \alpha) = 0 \quad (13)$$

where R_a and R_r are the reaction forces on the transition arms and rear wheels, respectively, e is the longitudinal distance between rear wheels' axes and the center of servo motor shafts, α is the rising angle of the robot measured from the ground plane, l is the transition arm length, β is the transition arm angle with the robot platform, and h is the orthogonal distance between the rear wheel centers and servo motor shaft centers. Table 6 presents the exact values of the transition mechanism parameters. The robot weight, W , should be confined within the region formed by the points of reactions with ground (i.e. R_a and R_r) during the entire transition process. The transition

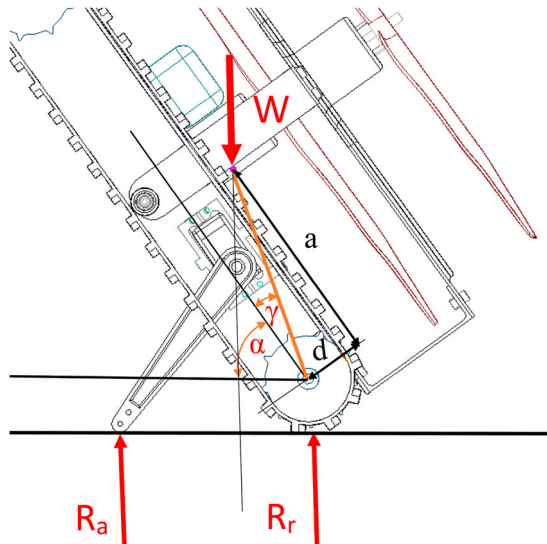


Figure 14. Transition arm analysis for critical arm angle.

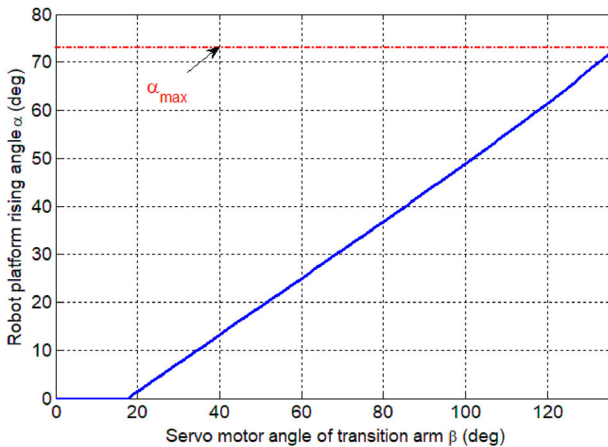


Figure 15. Relationship between the transition arm angle β and robot rising angle α .

stability is maintained by the following two conditions:

$$\cos(\alpha + \gamma)\sqrt{(a^2 + d^2)} > 0, \quad (14)$$

$$e \cos \alpha + l \cos(\beta - \alpha) - h \sin \alpha > a \cos \alpha, \quad (15)$$

where γ is the angle between the platform longitudinal direction and the line connecting center of rear wheels with the COM, as shown in Figure 14. It is given as; $\gamma = \tan^{-1}(d/a)$. Equation (14) is essential to avoid tipping backward by keeping the COM location at the left of R_r . Therefore, the critical rising angle α can be calculated from this formula. It is found that, $\alpha_{max} = 73.2^\circ$ before tipping around the rear wheels. Whereas, Equation (15) restricts the COM location to be always at the right of R_a in order to avoid tipping forward. The torque of each servo motor is obtained by the following equation:

$$T_{servo} = \frac{R_a}{2} l \cos(\beta - \alpha). \quad (16)$$

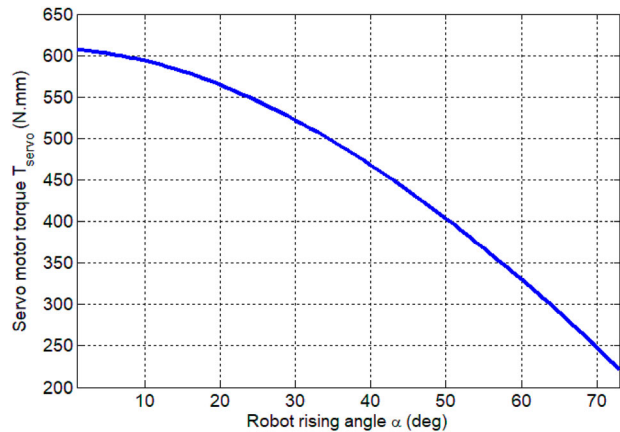


Figure 16. Relationship between the servo motor torque of transition arm T_{servo} and the rising angle α .

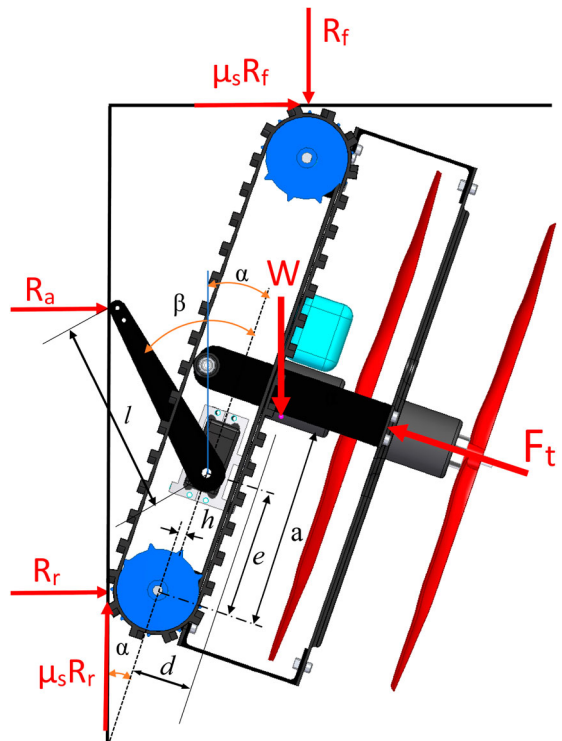


Figure 17. Wall-ceiling transition analysis.

Basically, from the transition mechanism geometry, one can get a relationship between α and β , as follows:

$$r + e \sin \alpha + h \sin(\alpha + 90) = l \sin(\beta - \alpha). \quad (17)$$

By specifying the length of the arms, as given in Table 6, the arm angle β can be defined at a certain rising angle α as shown in Figure 15. A practical relationship between α and the servo motor torque, T_{servo} , can be obtained by solving (13) and (16) and plotted, as shown in Figure 16. It shows that the maximum torque is applied at the beginning of transition which is 627.23 N mm.

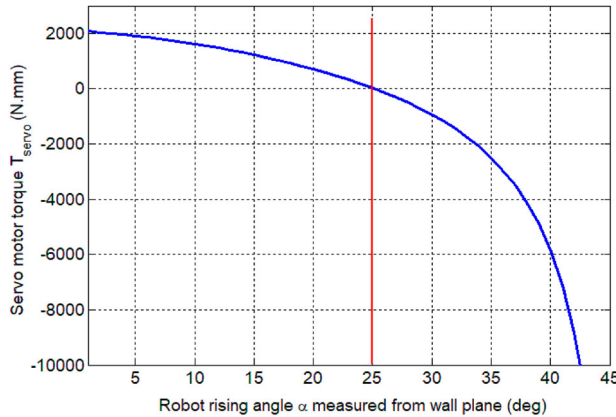


Figure 18. Servo motor torque of transition arm T_{Servo} versus the rising angle α , during wall-ceiling transition.

4.2. Wall-ceiling transition

Investigation of the wall-ceiling transition is very substantial for obtaining the maximum required torques of the transition arms. Subsequently, proper and minimum weight servo motors could be chosen. Not only the orientation of the robot changes with changing the transition arm angle, as the previous case, but also the robot location. This is due to the propellers' thrust forces which push the robot continuously to change its location. These thrust forces along with the transition arm torques will make the robot on the verge of transiting gradually between the wall and the ceiling. The free-body diagram shown in Figure 17 illustrates the equilibrium analysis of this system. The front and rear friction forces are taken as $\mu_s R_f$ and $\mu_s R_r$, respectively, since the robot is being on the verge of motion. The equations satisfying the equilibrium conditions are stated as follows:

$$F_t \cos \alpha - R_a - R_r - \mu_s R_f = 0 \quad (18)$$

$$F_t \sin \alpha - W + \mu_s R_r - R_f = 0 \quad (19)$$

$$\begin{aligned} & -W(r + a \sin \alpha + d \cos \alpha) + F_t \left(\frac{L}{2} + r \sin \alpha \right) \\ & -R_a[l \cos(\beta - \alpha) + e \cos \alpha - h \sin \alpha] \\ & -R_f(L \sin \alpha + r) - \mu_s R_f(L \cos \alpha + r) = 0, \end{aligned} \quad (20)$$

where R_f is the front reaction force, μ_s is the static friction coefficient, L is the distance between the front and rear wheels' axes. By solving the above Equations (18–20), one can get the torque of the transition arms from (16). Therefore, a relation between the required torque of each servo motor and the rising angle (α) can be obtained and plotted, as presented in Figure 18. It shows that the maximum torque is applied at the beginning of the transition, and it is equal to 2078 N mm. When the rising

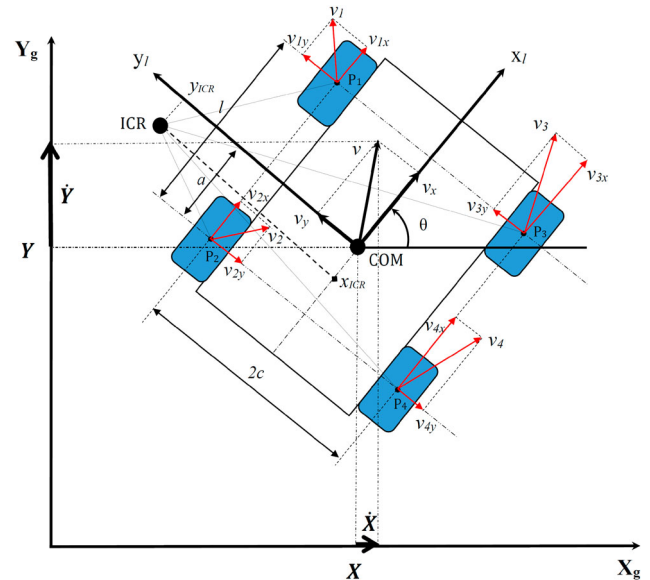


Figure 19. Representation of SSCR velocities with ICR on the climbed surface plan.

angle reaches a value of 25° , the torque becomes zero and decreases to a negative value. This means that the transition arms are not required anymore after this angle, and the thrust forces will be completely able to accomplish the transition task.

5. EJBot kinematics and dynamics model

Studying the kinematics and dynamics of EJBot is vital for its proper operation and control. Although the skidding effect between wheels and surface may be observed for all vehicles, only for the skid-steering vehicles it is necessary to change their heading. Moreover, in spite of the fact that skidding is necessary to change robot's orientation, extensive skidding causes instability of the motion, hence it is necessary to limit the velocity of the vehicle. Control problem for skid steering mobile robot (SSMR) is quite challenging, mainly because of two facts. Firstly, SSMR is an under-actuated system and secondly, its mathematical model is highly uncertain.

5.1. Kinematics of EJBot

Kinematics and dynamics models of EJBot as a skid-steering climbing robot (SSCR) were studied formerly by the authors in [26], where the steering is achieved by differentiable driving wheel pair on each side. Although this steering type gains some mechanical benefits of higher traction forces and transporting efficiently over difficult terrains, the control of SSCR is a challenging task because the wheels must skid laterally to follow a curved path, see

Figure 19. Therefore, the instantaneous center of rotation (ICR) is playing the main role in this modeling. Taking into account the position of ICR, one can find the following important relationship:

$$\frac{v_x}{y_{ICR}} = -\frac{v_y}{x_{ICR}} = \omega, \quad (21)$$

where v_x , v_y and ω are the longitudinal, lateral and angular velocities of the robot expressed in local frame $o_l(x_l y_l)$, respectively, x_{ICR} , y_{ICR} are the longitudinal and lateral projection of the ICR on the local frame. Consequently, in order to complete the kinematic model of the SSCR, the lateral constraint is imposed as follows:

$$v_y + \omega x_{ICR} = 0. \quad (22)$$

This equation is not integrable, and it describes a non-holonomic constraint which can be rewritten in the following form, [27], [28]:

$$[-\sin \theta \quad \cos \theta \quad x_{ICR}] [\dot{X} \quad \dot{Y} \quad \dot{\theta}]^T = A(\mathbf{q}) \dot{\mathbf{q}} = 0, \quad (23)$$

where $\mathbf{q} = [X \quad Y \quad \theta]^T$ is the generalized coordinates of the robot, where X and Y are the COM position, and θ is the orientation of the local frame with respect to the inertial frame around z_l . Then, $\dot{\mathbf{q}} = [\dot{X} \quad \dot{Y} \quad \dot{\theta}]^T$ denotes the vector of generalized velocities of the robot related to the inertial frame. Since the generalized velocity $\dot{\mathbf{q}}$ is always in the null space of A , then the kinematic model is derived as:

$$\dot{\mathbf{q}} = S(\mathbf{q}) \xi, \quad (24)$$

where $\xi = [v_x \quad \omega]^T$ is the robot velocity vector in local frame,

$$S^T(\mathbf{q}) A^T(\mathbf{q}) = 0, \quad (25)$$

and

$$S(\mathbf{q}) = \begin{bmatrix} \cos \theta & x_{ICR} \sin \theta \\ \sin \theta & -x_{ICR} \cos \theta \\ 0 & 1 \end{bmatrix}. \quad (26)$$

A control relationship in kinematic level between the angular velocities of the wheels and the robot velocities in the local frame can be derived as follows:

$$\xi = \begin{bmatrix} v_x \\ \omega \end{bmatrix} = \frac{r}{2} \begin{bmatrix} 1 & 1 \\ -\frac{1}{c} & \frac{1}{c} \end{bmatrix} \begin{bmatrix} \omega_L \\ \omega_R \end{bmatrix}, \quad (27)$$

where the pair of velocities ω_L and ω_R are the left and right wheels' angular velocities, respectively, and can be treated as a control kinematic input signal as well as

velocities v_x and ω , considering nonslip condition in longitudinal direction.

5.2. Dynamics of EJBot

The control of SSCR at kinematic level only is not enough and requires the utilization of a properly designed control algorithm at a dynamic level too. For simplification, it is assumed that the mass distribution of the robot is homogeneous and kinetic energy of the wheels and drives can be neglected. Therefore, the dynamic model of SSCR can be expressed as follows:

$$\bar{M} \ddot{\mathbf{q}} + \bar{C} \dot{\mathbf{q}} + \bar{F} + \bar{G} = \bar{B} \tau \quad (28)$$

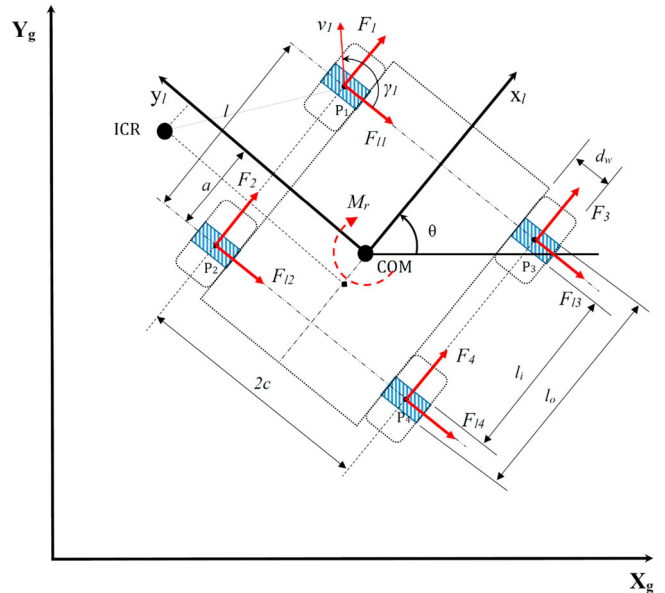


Figure 20. The resistive forces and moment acting on SSCR.

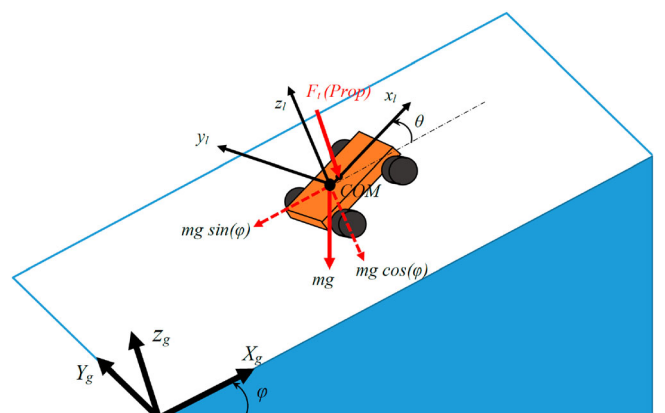


Figure 21. SSCR local and global frames on a ramp with inclination angle (ϕ).

where

$$\begin{aligned}\bar{M} &= \begin{bmatrix} m & 0 & 0 \\ 0 & m & 0 \\ 0 & 0 & I \end{bmatrix}, \quad \bar{C} = \begin{bmatrix} 0 & -m & 0 \\ m & 0 & 0 \\ 0 & 0 & 0 \end{bmatrix} \omega, \\ \bar{F} &= [0 \quad F_l \quad M_r]^T, \\ \bar{G} &= \begin{bmatrix} mg \sin \phi \cos \theta \\ -mg \sin \phi \sin \theta \\ 0 \end{bmatrix}, \quad \bar{B} = \frac{1}{r} \begin{bmatrix} 1 & 1 \\ 0 & 0 \\ -c & c \end{bmatrix}, \\ \boldsymbol{\tau} &= \begin{bmatrix} \tau_L \\ \tau_R \end{bmatrix} = \begin{bmatrix} \tau_1 + \tau_2 \\ \tau_3 + \tau_4 \end{bmatrix}\end{aligned}\quad (29)$$

where $\eta = [v_x \quad v_y \quad \omega]^T$ is the robot velocity vector, m and I denoting the mass and inertia of EJBot, \bar{F} is a vector consists of the resultant lateral resistive force on the wheels F_l , and the resistive moment around the center of mass M_r , see Figure 20, \bar{G} is the gravitational force vector, and $\boldsymbol{\tau}$ is the input torques' vector of the right and left wheels. It should be noted that determination of \bar{F} is quite difficult, where it results from sophisticated ground-wheel interaction. The model is characterized by the coefficient of friction, and the shear deformation modulus, which have terrain-dependent values. There are two methods to define the lateral resistive force F_{li} , discussed in details in [26], the first method based on Coulomb friction model as used in Kozlowski *et al.*, [28], and the second one based on the wheel-ground interaction theory depending on the shear stress between the wheels/tracks and the ground, as described by Wong, [29], [30], and [31]. Basically, the main target of EJBot is to climb structures with variable inclination angle ϕ , as

shown in Figure 21, therefore the potential energy resulting from the robot weight should be taken into consideration. The effect of gravity was neglected in Kozlowski *et al.* model, since their robot is considered a ground mobile robot, while EJBot climbs against the gravity. Hence, the gravitational term \bar{G} expressed in (29) is added to the dynamic equation. Since the extensive skidding results in unstable motion, the skidding effect should be described in detailed manner. Consequently, the dynamic model can be rewritten in the following form:

$$\begin{bmatrix} mv_x \\ mv_y \\ I\dot{\omega} \end{bmatrix} + \begin{bmatrix} -mv_y\omega \\ mv_x\omega \\ 0 \end{bmatrix} + \begin{bmatrix} 0 \\ F_l \\ M_r \end{bmatrix} + \begin{bmatrix} mg \sin \phi \cos \theta \\ -mg \sin \phi \sin \theta \\ 0 \end{bmatrix} = \begin{bmatrix} \frac{1}{r}(\tau_L + \tau_R) \\ 0 \\ \frac{c}{r}(-\tau_L + \tau_R) \end{bmatrix} \quad (30)$$

One can notice from the above equation that the longitudinal velocity v_x and angular velocity ω are controlled directly by the torque signals, whereas, the lateral velocity v_y is not related directly to the input torques. Instead of that, it is a function of wheel-ground interaction and product of longitudinal and angular velocities. Kozlowski and Pazderski [28] proposed a necessary condition to limit v_y to decrease the skidding magnitude by determining the lateral reactive forces F_l and wheel velocities v_{yi} based on the location of ICR as follows:

$$F_l = [-(\mu_{l2}F_{r2} + \mu_{l4}F_{r4})\hat{sgn}(x_{ICR} + a) + (\mu_{l1}F_{r1} + \mu_{l3}F_{r3})\hat{sgn}(-x_{ICR} + (l - a))] \hat{sgn}(\omega). \quad (31)$$

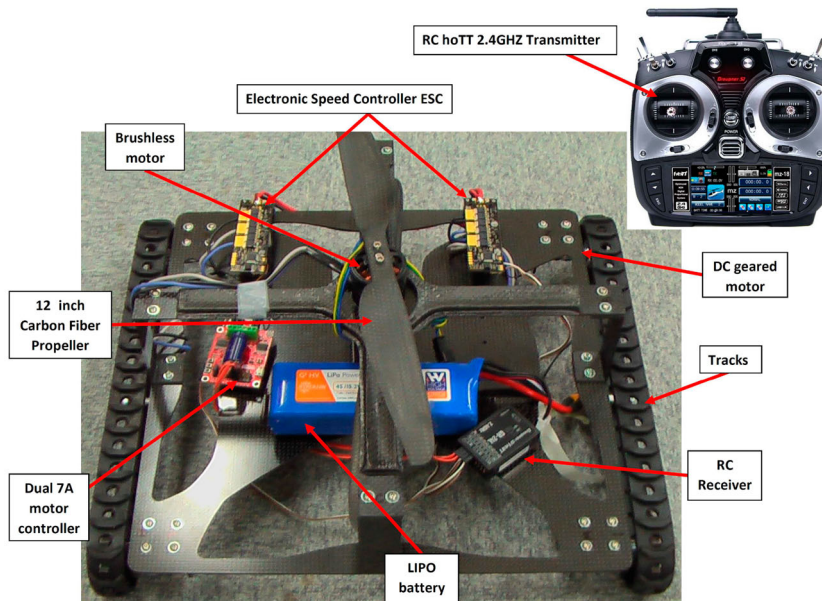


Figure 22. EJBot-II components.

The resultant lateral resistive forces F_l is strictly related to longitudinal location of ICR, (i.e. x_{ICR}), based on the following set:

$$F_l = \text{sgn}(\omega) \cdot \begin{cases} \sum_{i=1}^4 \mu_{li} F_{ri} & x_{ICR} < -a \\ \sum_{i=1,3} \mu_{li} F_{ri} & x_{ICR} = -a \\ -\sum_{i=2,4} \mu_{li} F_{ri} + \sum_{i=1,3} \mu_{li} F_{ri} & -a < x_{ICR} < l-a \\ -\sum_{i=2,4} \mu_{li} F_{ri} & x_{ICR} = l-a \\ -\sum_{i=1}^4 \mu_{li} F_{ri} & x_{ICR} > l-a \end{cases} \quad (32)$$

From equation (30), one can write:

$$\dot{v}_y = -v_x \omega - \frac{F_l}{m} + g \sin \phi \sin \theta \quad (33)$$

By taking a time derivation of equation (22), we get the following relationship:

$$\dot{v}_y = -\omega x_{ICR} - \dot{\omega} x_{ICR} \quad (34)$$

Hence, a linear differential equation is obtained by solving the above two equations together, as follows:

$$\omega \dot{x}_{ICR} + \dot{\omega} x_{ICR} = v_x \omega + \frac{F_l}{m} - g \sin \phi \sin \theta. \quad (35)$$

By simplifying the analysis and assuming that angular velocity is constant ($\dot{\omega} = 0$), then,

$$x_{ICR}(t) = x_{ICR}(t_0) + \int_{t_0}^t (v_x(\alpha) + \frac{F_l(\alpha)}{m \omega} - \frac{g}{\omega} \sin \phi \sin \theta) d\alpha. \quad (36)$$

This equation represents the solution of the nonholonomic constraint considering the dynamic change of x_{ICR} during the robot movement. For more details on the dynamic model of nonholonomic skid steering mobile robots, see [32], [33], and [34].

6. EJBot-II prototype and experiments

In this section, EJBot-II prototype is fabricated and assembled. It consists of four main systems. The first one is the thruster unit which includes two propellers, brushless motors, and electronic speed controller (ESC).

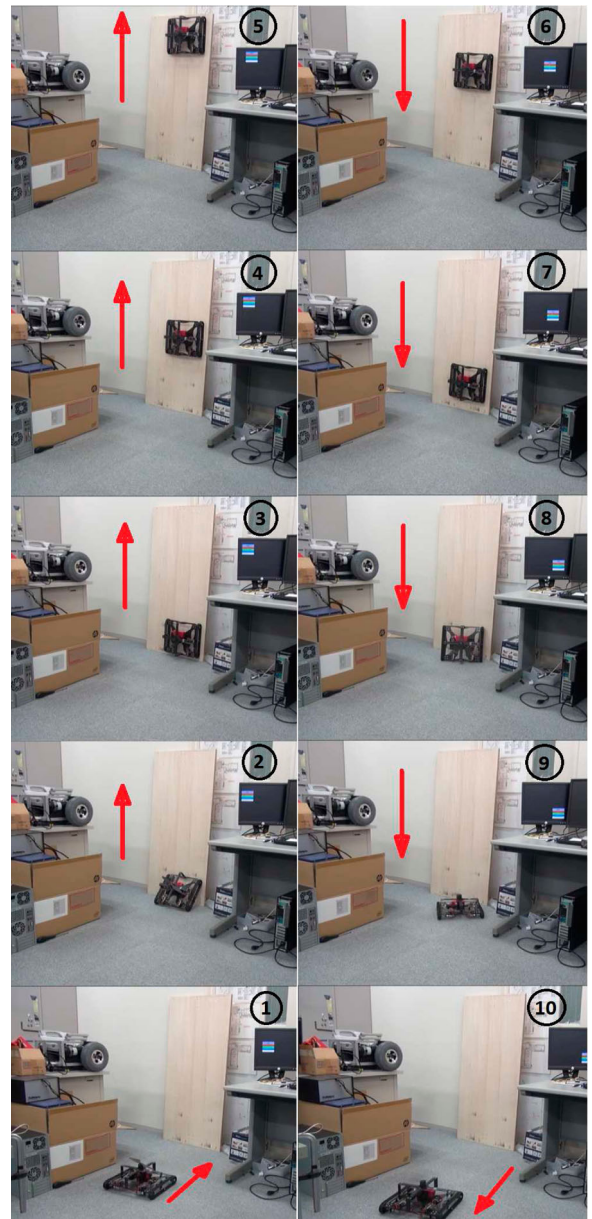


Figure 23. EJBot-II test for transition from ground to wall and climbing then getting down gain.

The second system is the driving and steering system which consists of two tracks, DC geared motors, and one DC dual motor driver (Roboclaw 2×7A). The third system is the transition mechanism which includes two servo motors and arms. The fourth system is the controller unit which is mainly based on a tele-operated radio control system consisting of 9-channel 2.4-GHz hoTT receiver and transmitter. The main robot components are shown in Figure 22. EJBot-II is supplied with power by a portable LIPO battery that has 6-cell and 3000 milli-Ampere-hour (mAh) capacity. Its mass is around 300 g and mounted directly on the robot platform for navigating any structure easily, especially the

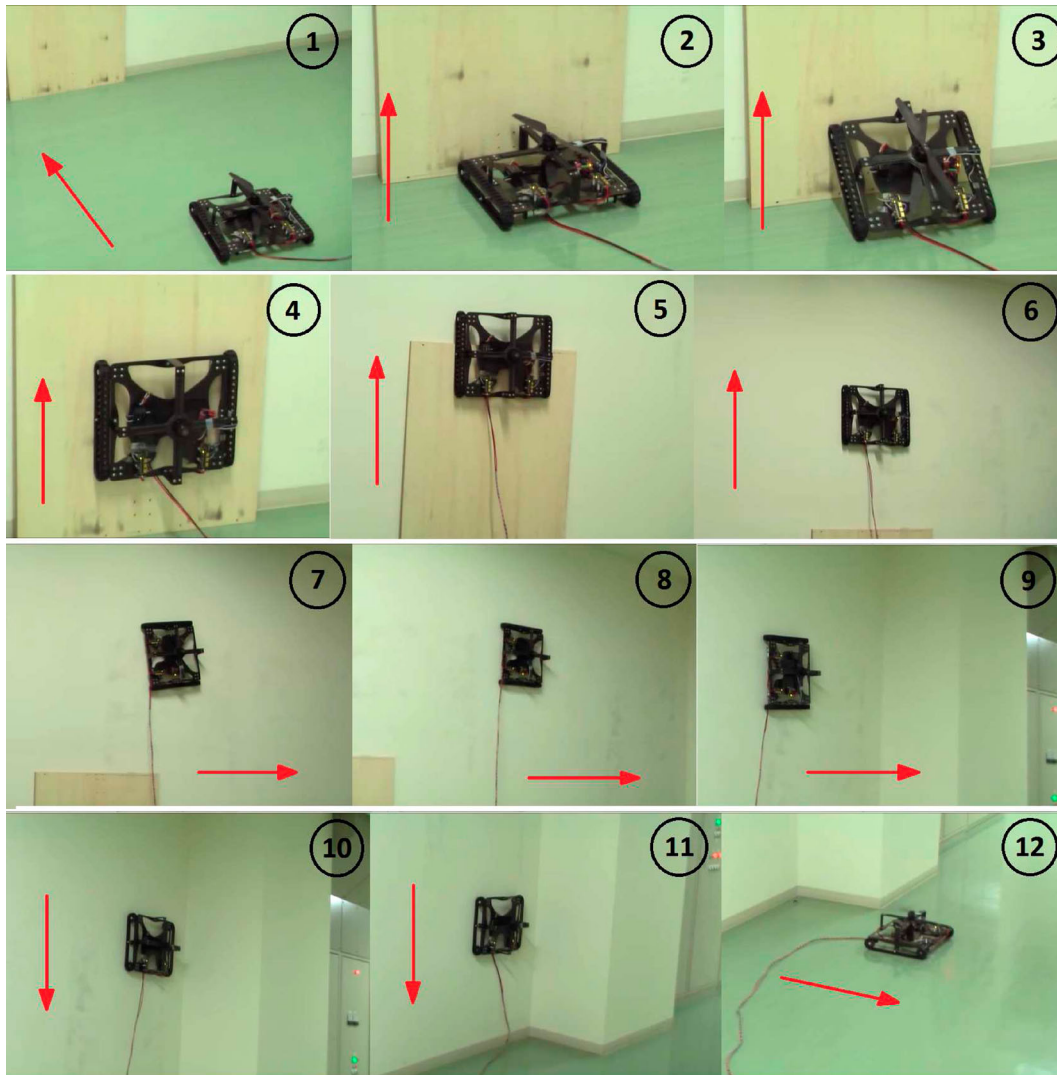


Figure 24. EJBot-II test on a smooth laboratory wall for the transition from ground to wall and climbing in different directions on the wall then getting down to the ground.

complex environment with a lot of obstacles. The battery provides the robot with a power enough to operate about 10–15 minutes. In case of using a battery with larger capacity, it is preferred to use a connecting cable, where a battery of 6-cell and 5000 mAh has a weight of 750 g. Consequently, this weight will reduce the robot payload capacity greatly. This high capacity battery can operate the robot around 45 minutes. So, it has a merit of long operation time and durability, even it has some cable issues.

The robot is tested to climb walls in the laboratory and to transit from the ground to walls directly. Some experimental tests are performed using the small battery mounted on the robot while others are performed using the big battery connected with a cable. The first test is performed to move on the ground and then climb a vertical wooden plate inside the lab and stop for about 12 seconds, and then, get down again to the ground, as shown

in Figure 23. The second test is accomplished to check the robot ability for climbing a smooth wall in the lab and moving in different directions on the wall. Figure 24 shows EJBot-II during climbing-up and moving in vertical and horizontal directions on the wall, and finally getting down again to the ground. Some wall surfaces have sufficient roughness to allow the robot tracks to transit automatically without aid of the transition arms like the previous examples. The third experiment is performed to check the transition on a slippery step in the wall that prevents the robot getting climb-up with only its tracks and propellers support. It is necessary to use the transition system with such cases. Figure 25 shows the transition process steps in details starting of approaching the wall until retracting the arms preparing for climbing-up. The robot takes a simple strategy based on actuating the arm servo motors with a certain angle (*i.e.* 80° with respect to their rest position). This makes the robot's tip

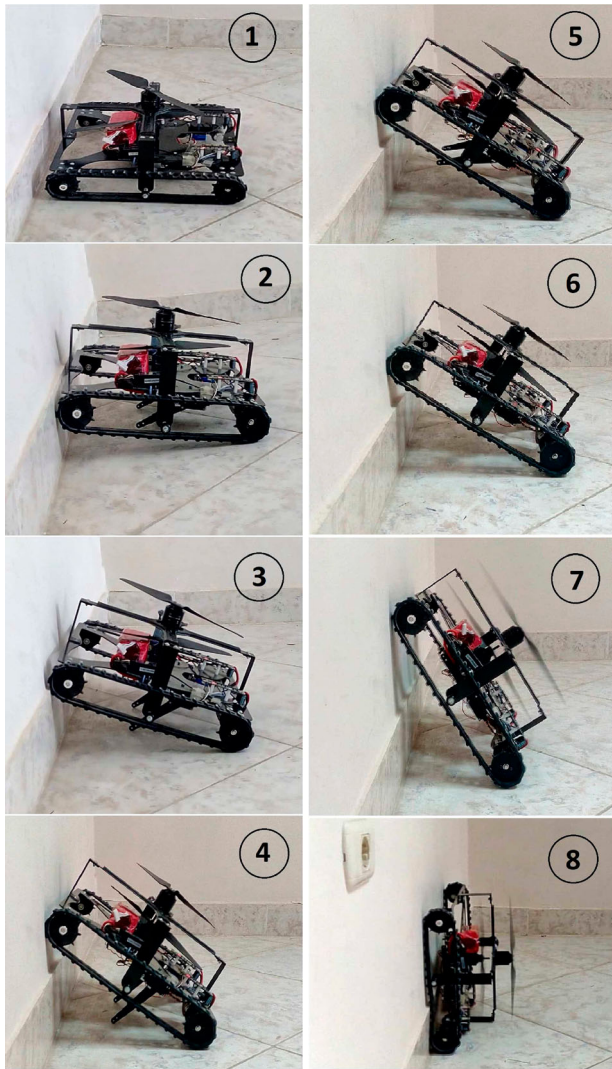


Figure 25. Transition strategy for tackling a slippery step on the wall.

raised up, then the tracks move to let the robot touch the wall and lean on it. Hence, this position permits the robot to retract the arms and continue climbing easily. These overall experimental tests demonstrate EJBot-II's ability to transit between the floor and walls easily, and exploring smooth wall surfaces efficiently, as well as, stopping accurately on these walls. It is noticed that EJBot-II can hold on the wall accurately even the torques of track wheels are deactivated. This is due to the high friction forces on the rubber tracks, unlike the EJBot-I wheels which should be supplied with a constant torque to stop it at its place on the wall. This gives EJBot-II advantageous feature and easiness in the control and use.

7. Conclusion

This article presents a new model of a propeller-type climbing robot called EJBot-II. It is considered an

important enhancement of the first prototype (EJBot-I), where the weight is optimized and the climbing performance is greatly improved. The robot shows a good transition between the intersected surfaces. EJBot-II gets its power from a portable LIPO battery without using umbilical cables for good applicability in the industrial fields. The robot is tele-operated by 9-Chanel radio control system. By using the vision system the robot can be controlled efficiently inside the industrial vessels. There still many experiments to be achieved, such as climbing real petrochemical vessels. Many sensors shall be installed on the robot such as; orientation, IMU, and ultrasonic sensors, besides a wireless camera for visual inspection and wall thickness sensor for the inspection of petrochemical vessels. All these suggested enhancements are going to be implemented in the future works. This will make the robot fully automated and more functional for the industrial field purposes.

Acknowledgments

Thanks go to Nikki Fron Company at Tokyo for their support in fabricating CFRP frame of EJBot-II. The authors are so grateful to Prof. Krister Svanberg from the Royal Institute of Technology, Stockholm for providing us with his MMA Matlab code.

Disclosure statement

No potential conflict of interest was reported by the authors.

Funding

The authors gratefully acknowledge Cultural Affairs and Missions Sector, Ministry of Higher Education (MoHE), Egypt, as well as, SHALAB, Shuji Hashimoto Lab, Waseda University, Tokyo, for funding EJBot-II project.

Notes on contributors

Mohamed G. Alkalla has received his B.E. and M.Sc. degrees in Mechanical Design Engineering from Production Engineering and Mechanical Design Department, Faculty of Engineering, Mansoura University, Egypt, in 2007 and 2013, respectively. He was a visiting research fellow at SHALAB Laboratory, Department of Applied Physics, Waseda University, Tokyo, Japan in 2016. He has received his Ph.D. in Mechatronics and Robotics Engineering at Egypt-Japan University of Science and Technology (E-JUST), Alexandria, Egypt in 2017. He is Assistant Professor at Production Engineering and Mechanical Design Department, Faculty of Engineering, Mansoura University, Egypt, since 2017. He is currently working as a Research Fellow at Surrey Space Centre, University of Surrey, UK with a FAIR-SPACE Hub team on Artificial Intelligent Robotic Systems for Space. His major research interests include robotics,

mechanical design, mechatronic systems, and structural optimization. The recent publications focused on climbing robots, topology optimization, and extraterrestrial drilling systems.

Mohamed Fanni has received his B.E. and M.Sc. degrees in Mechanical Engineering from Faculty of Engineering of both Cairo University and Mansoura University, Egypt, in 1981 and 1986, respectively. He has received the Ph.D. degree in Engineering from Karlsruhe University, Germany, 1993. He currently occupies a Professor position in the Department of Mechatronics and Robotics Engineering, at Egypt-Japan University of Science and Technology (E-JUST), Alexandria, on leave from Production Engineering and Mechanical Design Department, Faculty of Engineering, Mansoura University, Egypt. His major research interests include robotics engineering, automatic control, and Mechanical Design. His current researches focus on Design and Control of Mechatronic Systems, Surgical Manipulators, Industrial Robots and Flying/Walking Robots.

Abdelfatah M. Mohamed: Has received the Ph.D degree from University of Maryland, College park, USA in 1990. Since 1990 he has been an Assistant Professor at the Dept. of Electrical Engineering, Assiut University. He became an Associate Professor in 1995, and Professor in 2000. From September 1990 to August 1993, He has been a Postdoctoral Fellow at the Dept. of Mechanical Engineering, University of Texas at Austin USA. From April 1996 to April 1997, He has been a visiting Professor at the Dept. of Electrical Engineering, Kanazawa University Japan. From September 2010 to March 2012 He has been the Head, Dept. of Electrical Engineering, Assiut University, Egypt. From April, 2012 to September 2013 He has been the Dean of Faculty of Engineering, Assiut University, Egypt. From November 2013 to September 2018, he has been the head of the Dept. of Mechatronics and Robotics Engineering, Egypt-Japan University of Science & Technology. Currently, he is a Professor at the Dept. of Mechatronics and Robotics Engineering, Egypt-Japan University of Science & Technology. His research interest lies in Robust and Intelligent control of Magnetic Bearing, Magnetic Levitation systems, Robotics, Industrial drives and Power systems. Dr. Mohamed is a senior IEEE member. Google scholar h-index = 13.

Shuji Hashimoto, Dr. Eng. (Member, IEEE) received the B.S., M.S. and Dr. Eng. degrees in Applied Physics from Waseda University, Tokyo, Japan, in 1970, 1973 and 1977, respectively. He is currently a Emeritus Professor in the Department of Applied Physics, School of Science and Engineering, Waseda University. Since 2000, he has been a director of the Humanoid Robotics Institute, Waseda University. From 1979 to 1991, he was with the Faculty of Science, Toho University, Funabashi. He was a Vice President of International Computer Music Association until 2001. He is the author of over 200 technical publications, proceedings, editorials and books. He is a reviewer for many journals and conferences on computer music, computer vision, robotics and neural computing. His research interests are in human communication and Kansei information processing including image processing, music systems, neural computing and humanoid robotics. From 2003, he serves as chair of the promotion committee, IEEE Tokyo Section. Membership of professional institutions: IEEE, ICMA (International Computer Music Association), IEICE (Institute

of Electronics, Information and Communication Engineers), IPSJ(Information Processing Society of Japan), SICE(The Society of Instrument and Control Engineers), ISCIE, I.I.E.E.J (Institute of Image Electronics Engineers of Japan), RSJ (The Robotics Society of Japan), Human Interface Society of Japan, and Virtual Reality Society of Japan.

Hideyuki Sawada is a Professor in the Department of Applied Physics, Faculty of Science and Engineering, Waseda University. He received the B.E., M.E. and Ph.D. degrees in Applied Physics from Waseda University in 1990, 1992 and 1999, respectively. In 1999, he joined the Department of Intelligent Mechanical Systems Engineering, Faculty of Engineering, Kagawa University, as an Associate Professor, and became a Professor in 2010. His current research interests include robotics, sound and image processing, machine learning, human interfaces, and tactile sensing and display.

Takanobu Miwa has received his Ph.D in engineering from Waseda University, Tokyo, Japan, in 2017. He has been a research associate at the Faculty of Science and Engineering, Waseda University from April 2015 to March 2018. Currently, he is working as a science teacher at Chuo University Junior and Senior High School which is designated as a Super Science High School by the Ministry of Education, Culture, Sports, Science and Technology (MEXT). His research interests include scientific visualization, human-computer interaction, robotics, and physics education.

Amr Hamed received the B.S. degree in Electronics and Communication Engineering and M.Sc. degree in Electronics Engineering from Benha University, Egypt, in 2011 and 2015, respectively. He is currently pursuing the Ph.D. degree in Mechatronics and Robotics Engineering at Egypt-Japan University of Science and Technology.

ORCID

Mohamed G. Alkalla  <http://orcid.org/0000-0001-5264-3292>

References

- [1] Alkalla MG, Fanni MA, Mohamed AF. Versatile climbing robot for vessels inspection. 2015 International Conference on Control, Automation and Robotics (ICCAR); 2015 May; p. 18–23.
- [2] Alkalla M, Fanni M, Mohamed A. A novel propeller-type climbing robot for vessels inspection. 2015 IEEE International Conference on Advanced Intelligent Mechatronics (AIM); 2015 July; p. 1623–1628.
- [3] Alkalla MG, Fanni MA, Mohamed AM, et al. Tele-operated propeller-type climbing robot for inspection of petrochemical vessels. Ind Robot: Int J. 2017;44(2): 166–177. doi:10.1108/IR-07-2016-0182
- [4] Ge D, Ren C, Matsuno T, et al. Guide rail design for a passive suction cup based wall-climbing robot. 2016 IEEE/RSJ International Conference on Intelligent Robots and Systems (IROS); 2016 Oct; p. 5776–5781.
- [5] Zhu H, Guan Y, Wu W, et al. Autonomous pose detection and alignment of suction modules of a biped wall-climbing robot. IEEE ASME Trans Mechatron. 2015 April;20(2):653–662.

- [6] Yuan YY, Lu WC, Kao CJ, et al. Design and implementation of an inchworm robot. 2016 International Conference on Advanced Robotics and Intelligent Systems (ARIS); 2016 Aug; p. 1–1.
- [7] Lee G, Kim H, Seo K, et al. Multitrack: a multi-linked track robot with suction adhesion for climbing and transition. *Robot Auton Syst*. **2015**;72:207–216.
- [8] Tramacere F, Beccai L, Mattioli F, et al. Artificial adhesion mechanisms inspired by octopus suckers. 2012 IEEE International Conference on Robotics and Automation; 2012 May; p. 3846–3851.
- [9] Zhang H, Wang W, Gonzlez-Gmez J, et al. Design and realization of a novel modular climbing caterpillar using low-frequency vibrating passive suckers. *Adv Robot*. **2009**;23(7–8):889–906. doi:10.1163/156855309X442990.
- [10] Nejadfar A, Schütz S, Schmidt D, et al. Design of a stable controller for the climbing robot CREA. Springer International: Cham; **2016**; p. 165–178. doi:10.1007/978-3-319-26453-0_10.
- [11] Schmidt D, Hillenbrand C, Berns K. Omnidirectional locomotion and traction control of the wheel-driven, wall-climbing robot, cromsci. *Robot J*. **2011**;29(7):991–1003.
- [12] Hillenbrand C, Schmidt D, Berns K. Cromsci: development of a climbing robot with negative pressure adhesion for inspections. *Ind Robot: Int J*. **2008**;35(3):228–237. doi:10.1108/01439910810868552.
- [13] Bonaccorso F, Longo D, Muscato G. Modelling of an innovative actuator for climbing robot adhesion. 12th International Conference on Climbing and Walking Robots (CLAWAR); World Scientific; **2009**.
- [14] Xiao J, Sadegh A. City-climber: a new generation wall-climbing robots. Climbing and walking robots: towards new applications. InTech. 2007.
- [15] Koo IM, Trong TD, Lee YH, et al. Development of wall climbing robot system by using impeller type adhesion mechanism. *J Intell Robot Syst*. **2013**;72(1):57–72.
- [16] Lee J, Kim S. Suction based wall climbing robot for edge movement. Springer: Dordrecht; **2014**; p. 687–696. doi:10.1007/978-94-017-8798-7_79
- [17] Beardsley P. VertiGo a wall-climbing robot including ground-wall transition [cited 2015 Dec 29]. Available from: <https://www.disneyresearch.com/publication/vertigo/>.
- [18] Nishi A, Miyagi H. Propeller type wall-climbing robot for inspection use. Proc 10th Int Symp, on Automation and Robotics in Construction (ISARC). 1993; p. 189–196.
- [19] Nishi A, Miyagi H, Ishihara K. Development of wall inspection robots. Proc 12th Int Symp, on Automation and Robotics in Construction (ISARC). 1995; p. 103–108.
- [20] Tovar A, Patel NM, Niebur GL, et al. Topology optimization using a hybrid cellular automaton method with local control rules. *J Mech Des*. **2006**;128(6):1205–1216.
- [21] Bendsoe MP, Sigmund O. Topology optimization – theory, methods and applications, handbook. Berlin: Springer-Verlag; **2003**; p. 1–13.
- [22] Svanberg K. The method of moving asymptotes new method for structural optimization. *Int J Numer Methods Eng*. **1987**;24(2):359–373.
- [23] Tovar A, Khandelwal K. Topology optimization for minimum compliance using a control strategy. *Eng Struct*. **2013**;48:674–682. <http://www.sciencedirect.com/science/article/pii/S0141029612006219>
- [24] Sigmund O, Maute K. Topology optimization approaches. *Struct Multidiscipl Optim*. **2013**;48(6):1031–1055. doi:10.1007/s00158-013-0978-6
- [25] Torayca industries, inc. of carbon fiber reinforced polymer [cited 2017 Jan 15]. Available from: <http://www.torayca.com/en/>.
- [26] Fanni MA, Alkalla MG, Mohamed AM. Propeller type skid steering climbing robot based on a hybrid actuation system. *Int J Robot Autom*. **2018**;33(3). doi:10.2316/Journal.206.2018.3.206-5017
- [27] Kozłowski K, Pazderski D. Modeling and control of a 4-wheel skid-steering mobile robot. *Int J Appl Math Comput Sci*. **2004**;14(4):477–496.
- [28] Kozłowski K, Pazderski D. Practical stabilization of a skid-steering mobile robot – a kinematic-based approach. In: 2006 IEEE International Conference on Mechatronics; 2006 July; p. 519–524.
- [29] Wong J, Preston-Thomas J. On the characterization of the shear stress-displacement relationship of terrain. *J Terramech*. **1983**;19(4):225–234.
- [30] Wong J, Chiang C. A general theory for skid steering of tracked vehicles on firm ground. *Proc Inst Mech Eng Part D: J Autom Eng*. **2001**;215(3):343–355.
- [31] Wong JY. Theory of ground vehicles. New York: John Wiley & Sons; **2008**.
- [32] Fierro R, Lewis FL. Control of a nonholonomic mobile robot: backstepping kinematics into dynamics. *J Robot Syst*. **1997**;14(3):149–163. doi:10.1002/(SICI)1097-4563(199703)14:3 < 149::AI D-ROB1 > 3.0.CO;2-R
- [33] Pazderski D, Kozłowski K, Dixon W. Tracking and regulation control of a skid steering vehicle. American nuclear society tenth international topical meeting on robotics and remote systems; Citeseer; 2004. p. 369–376.
- [34] Yu W, Chuy Jr OY, Collins Jr EG, et al. Analysis and experimental verification for dynamic modeling of a skid-steered wheeled vehicle. *IEEE Trans Robot*. **2010**;26(2):340–353.